We are IntechOpen,
the world's leading publisher of Open Access books
Built by scientists, for scientists

6,900
Open access books available

185,000
International authors and editors

200M
Downloads

154
Countries delivered to

Our authors are among the

TOP 1%
most cited scientists

12.2%
Contributors from top 500 universities

CLARIVATE ANALYTICS
BOOK CITATION INDEX
INDEXED

WEB OF SCIENCE™

Selection of our books indexed in the Book Citation Index
in Web of Science™ Core Collection (BKCI)

Interested in publishing with us?
Contact book.department@intechopen.com

Numbers displayed above are based on latest data collected.
For more information visit www.intechopen.com

Chapter

Heat and Mass Transfer of Additive Manufacturing Processes for Metals

Zhengying Wei and Jun Du

Abstract

Additive manufacturing (AM), a method in which a part is fabricated layer by layer from a digital design package, provides the potential to produce complex components at reduced cost and time. Many techniques (using many different names) have been developed to accomplish this via melting or solid-state joining. However, to date, only a handful can be used to produce metallic parts that fulfill the requirements of industrial applications. The thermal physics and weld pool behaviors in metal AM process have decisive influence on the deposition quality, the microstructure and service performance of the depositions. Accurate analysis and calculation of thermal processes and weld pool behaviors are of great significance to the metallurgy analysis, stress and deformation analysis, process control and process optimization etc. Numerical modeling is also a necessary way to turn welding from qualitative description and experience-based art into quantitative analysis- and science-based engineering branch. In this chapter, two techniques for producing metal parts are explored, with a focus on the thermal science of metal AM: fluid flow and heat transfer. Selective laser melting (SLM) is the one that is most widely used because it typically has the best resolution. Another is named metal fused-coated additive manufacturing (MFCAM) that is cost competitive and efficient in producing large and middle-complex components in aerospace applications.

Keywords: additive manufacturing, selective laser melting (SLM), metal fused-coated additive manufacturing (MFCAM), fluid flow, heat transfer

1. Introduction

As a kind of advanced manufacturing technology, additive manufacturing (AM) provides an effective and 'bottom up' manufacturing where a complex structure can be built into its designed shape by a 'layer-by-layer' approach, which can directly create geometric metal parts. AM is versatile, flexible, highly customizable and, as such, can suite most sectors of industrial production [1]. Even though metal additive manufacturing involves creating parts layer-by-layer, there are many different types, including material extrusion, material jetting, material droplet printing, binder jetting, sheet lamination, powder bed fusion, and directed energy deposition [2]. Most current metal AM systems are of the powder bed fusion type [3]. Due to the complexity of the physical process in the process of metal AM, it is

very difficult to ascertain metal parts with high dimensional accuracy, no defects, small residual stress/deformation, compact microstructure and high mechanical properties [4–8]. At present, defect control and microstructure/composition control are key bottleneck problems that restrict the further development of metal AM technology. Both of these problems are closely related to the energy and mass transport process in deposition process, especially at the solid-liquid interface of molten pool [9–12]. How to understand and control the complex heat and mass transport in the molten pool is the key trend of the current research, and it is also the basis and prerequisite to break through the current technical bottlenecks and further improve the mechanical properties of the parts, such as strength, stiffness and fatigue. Therefore, this paper focuses on the scientific issues of transport phenomena and solidification behavior of molten pool during metal additive manufacturing.

2. Effect of processing parameters on forming defects during selective laser melting of AlSi10Mg powder

Selective laser melting is one of the most promising additive manufacturing processes. The randomly distributed packed powder particle is obtained using discrete element method (DEM) in PFC software. The correlation between the processing parameters (i.e., laser power, scanning speed, hatch spacing, and layer thickness) and the pores formation for the SLM-processed AlSi10Mg components was disclosed by simulations.

2.1 Numerical model

SLM process is complicated, involving heat transfer, evaporation, melting and solidification, re-melting and re-solidification, shrinkage and other thermophysical behaviors. In the numerical calculation model, in order to simplify the complicated physical process, the following assumptions need to be made: (1) The molten pool liquid is assumed as laminar and incompressible Newtonian fluid. (2) Mushy zone is treated as an isotropic permeability of porous medium in solid-liquid phase change. (3) Powder size is Gaussian distribution with sphere shape.

2.1.1 Establishment of randomly packed powder bed

A DEM-based randomly packed powder model was established by commercial platform PFC [13, 14]. In DEM, the contact between powder particles is regarded as a linear model while the mini deformations are allowable between the particles [15]. The linear force induced by the mini deformation could be regarded as the force exerted by a linear spring. The spring has a constant normal and shear stiffness, K_n and K_s [16]. In **Figure 1**, F_i, the contact force vector, is decomposed into two subvectors as F_n and F_s in the normal and shear direction, respectively. The stacking of the powder particles is accomplished by setting gravitational force until the powder particles reaches equilibrium. The powder bed porosity is set as 0.45, which is close to 0.5 which is the theoretical packing density. More details about the establishment of powder bed can be found in Refs. [13, 14].

As shown in **Figure 2**, two dense packing of Gaussian-sized spherical particles with dimensions of $500 \times 200 \times 35$ and $600 \times 300 \times 35$ μm were obtained by PFC with the parameters: the layer thickness of particles of 35 μm, the height of substrate of 30 μm. Then the powder bed model was converted to STL format for subsequent numerical simulation.
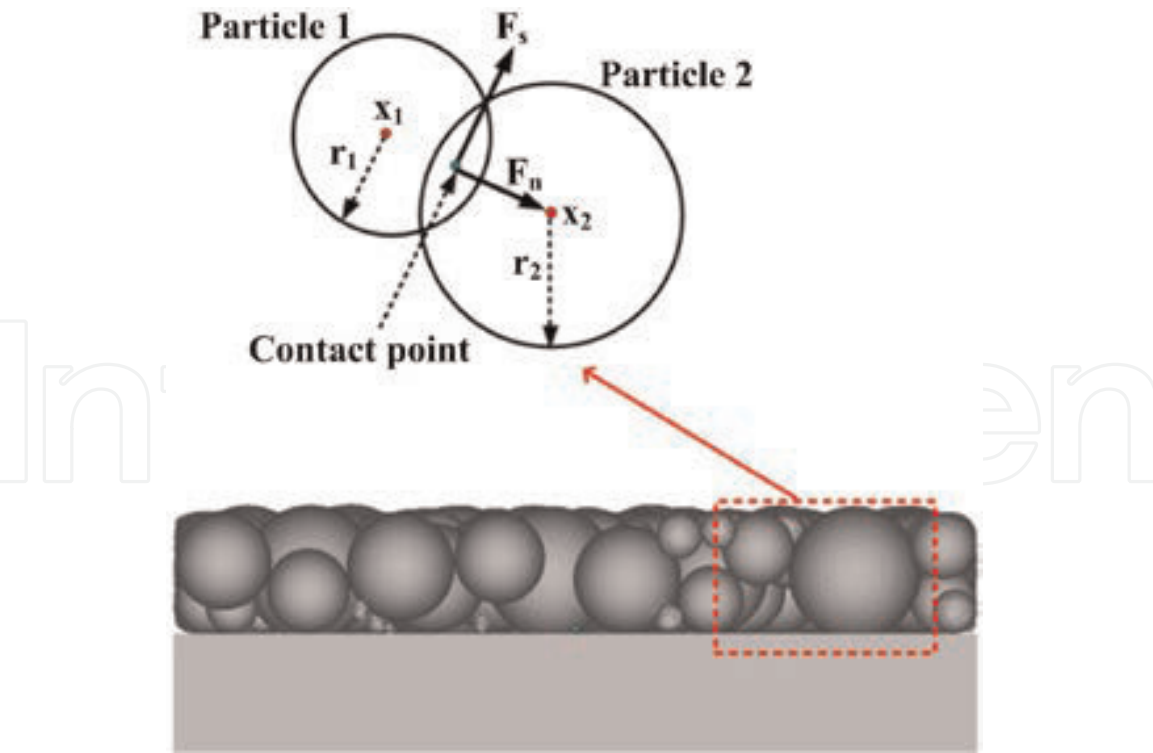
Figure 1.
Contact forces generated by interaction between two spherical particles x_1/x_2 and r_1/r_2 are the center and radius of particle 1 and particle 2, respectively.
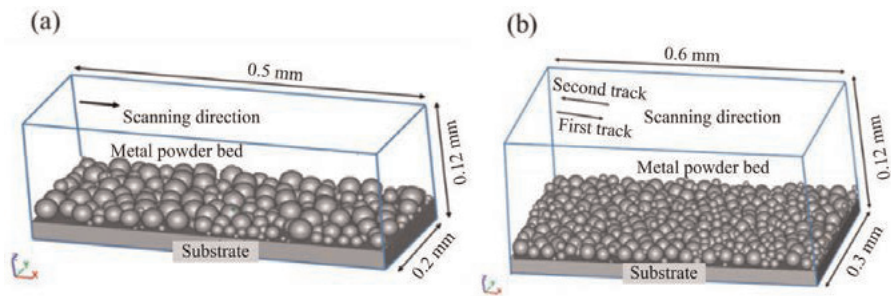

Figure 2.
Model of randomly packed AlSi10Mg powder bed. (a) Single track simulation, (b) multi-tracks simulation.

2.1.2 Conservation equations

The melt fluid flow is governed by N-S equations. The fluid free surface is captured employing the volume of fluid (VOF) method. The melt flow could be solved by the conservations of mass, momentum and energy, given by Eqs. (1)–(3), respectively.

Mass

$$\nabla \cdot \vec{V} = 0 \tag{1}$$

Momentum

$$\frac{\partial \vec{V}}{\partial t} + \left(\vec{V} \cdot \nabla \right) \vec{V} = -\frac{1}{\rho} \nabla P + \mu \nabla^2 \vec{V} + \vec{g} \left[1 - \beta(T - T_m) \right] \tag{2}$$

Energy

$$\frac{\partial H}{\partial t} + \left(\vec{V} \cdot \nabla \right) H = \frac{1}{\rho} (\nabla \cdot k \nabla T) + S_U \tag{3}$$

where $\vec{V}$ is velocity of the melt, ρ is the liquid metal density, P represents hydrodynamic pressure, μ is liquid viscosity, $\vec{g}$ is the gravitational acceleration, β is volumetric thermal expansion coefficient of the material, T represents the fluid temperature, T_m represents the melting temperature of AlSi10Mg.

The VOF method as shown in **Figure 3** was employed to track the free surface of the particles model obtained by DEM as they are melted, and it defined a function of the fraction of fluid by the following equation [17].

$$\frac{\partial F}{\partial t} + \nabla \cdot \left(\vec{V} F \right) = 0 \tag{4}$$

where F is the volume fraction of the liquid in a cell. When the cell is filled with liquid, $F = 1$; when the cell is void, $F = 0$. The value of F is between 0 and 1 when both the void and liquid are in the cell.

In this work, the laser energy of the AlSi10Mg powder bed was defined as 0.18 [18].

2.1.3 Boundary conditions

The heat-flux boundary condition at fluid free surface was given by [19].

$$\kappa \frac{\partial T}{\partial z} = q(r) - h_c (T - T_0) - \varepsilon_r \sigma_s \left(T^4 - T_0^4 \right) - q_{ev} \tag{5}$$

where h_c is the heat transfer coefficient, ε_r is the emissivity, σ_s is Stefan-Boltzmann constant, T_0 is ambient temperature, and q_{ev} is the heat loss by melt evaporation.

In SLM process, the liquid metal evaporation is given by the equation [20]

$$q_{ev} = 0.82 \frac{\Delta H^*}{\sqrt{2\pi MRT}} P_0 \exp \left(\Delta H^* \cdot \frac{T - T_{lv}}{RTT_{lv}} \right) \tag{6}$$

where M represents the molar mass, R is the ideal gas constant, P_0 represents the ambient pressure, T_{lv} is the boiling point of the metal melt, and ΔH^* is the effective enthalpy of loss metal vapor.
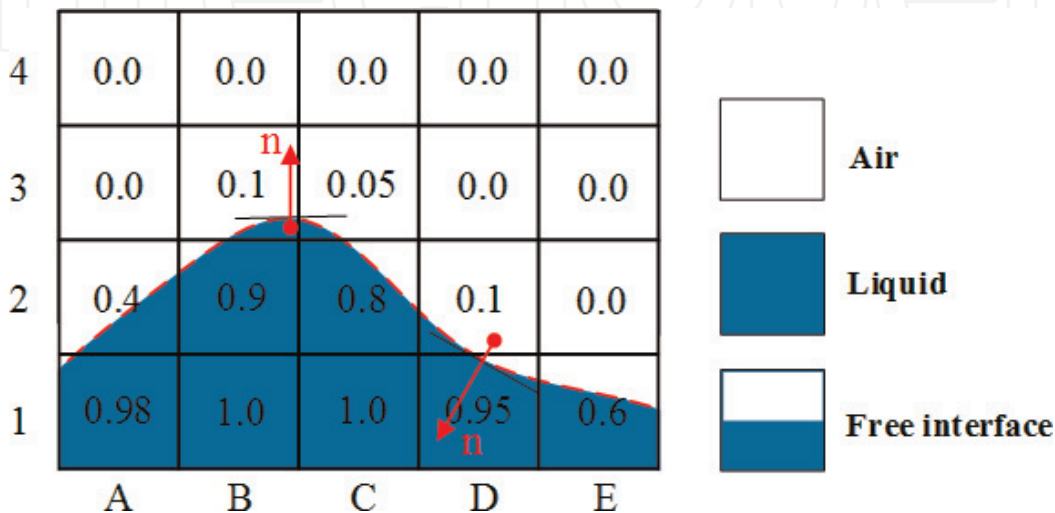

Figure 3.
Schematic diagram of VOF.

In order to simulate the Marangoni effect induced by the temperature gradient of the molten pool fluid, the shear stress should be balanced with boundary condition at fluid free surface, as given by [21]:

$$-\mu\frac{\partial u}{\partial z} = \frac{\partial \gamma}{\partial T}\frac{\partial T}{\partial x}$$
$$-\mu\frac{\partial v}{\partial z} = \frac{\partial \gamma}{\partial T}\frac{\partial T}{\partial y} \tag{7}$$

where $\partial\gamma/\partial T$ is the surface tension gradient. The surface pressure boundary condition including the surface normal force was given by [22]:

$$-P + 2\mu\frac{\partial \vec{v}_n}{\partial n} = -P_r + \sigma\left(\frac{1}{R_x} + \frac{1}{R_y}\right) \tag{8}$$

where $\vec{v}_n$ represents the normal velocity vector, P_r is the recoil pressure, σ means the surface tension, R_x and R_y represent the principal radius of surface curvature.

$$P_r = 0.54 P_0 \exp\left(L_{lv} \cdot \frac{T - T_{lv}}{RTT_{lv}}\right) \tag{9}$$

2.2 Material physical properties and numerical simulation

The AlSi10Mg powder (Felcon, China) used in SLM was produced by gas atomization. The chemical composition of the AlSi10Mg alloy is shown in **Table 1**. Drying the powder before laser melting by the drying ovens at temperature of 373 K can help reduce the humidity and the oxygen content within the powder. The scanning electron microscope (SEM) morphology of the AlSi10Mg powder is shown in **Figure 4a**, showing the morphology of powder particles is almost spherical. The powder particle size distribution was obtained by laser particle size analyzer (Sympatec, HELOS, Germany). In **Figure 4b**, the powder particle size is from 0 to 45 μm with the average size of 26.53 μm.

The thermophysical properties of AlSi10Mg and laser processing parameters are shown in **Figure 5** and **Table 2**. The temperature-dependent surface tension can be expressed as [23].

$$\sigma = 1000.726 - 0.152T \quad \text{When T} > T_l. \tag{10}$$

In this work, the final meshing of the model ensured the convergence of the simulation with the cell size of 2 μm. The minimum time step was defined as e^{-15} second while the maximum time step was defined as e^{-8} s. Implicit method was selected for the solvers of heat transfer, viscosity and surface tension. Explicit method was selected for free surface pressure solver. Numerical simulations were carried out on the commercial CFD platform Flow3D [13, 14].

Elements	Si	Mg	Fe	Cu	Ni	Zn	Pb	Sn	Ti	Al
wt.%	10.1	0.4	0.3	<0.05	0.03	0.05	0.03	0.03	0.01	Balance

Table 1.
Composition of AlSi10Mg (wt.%).
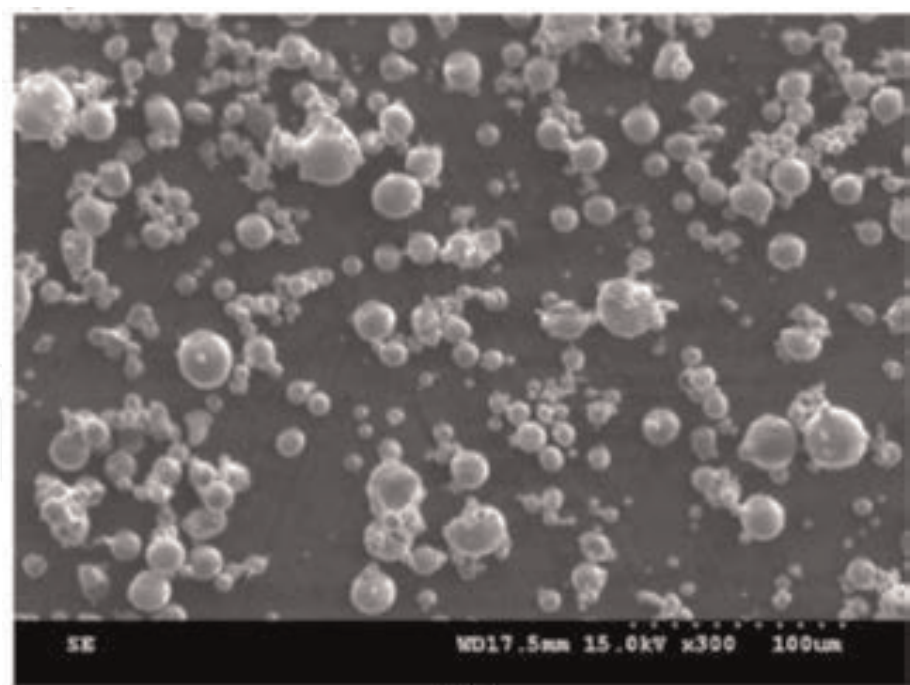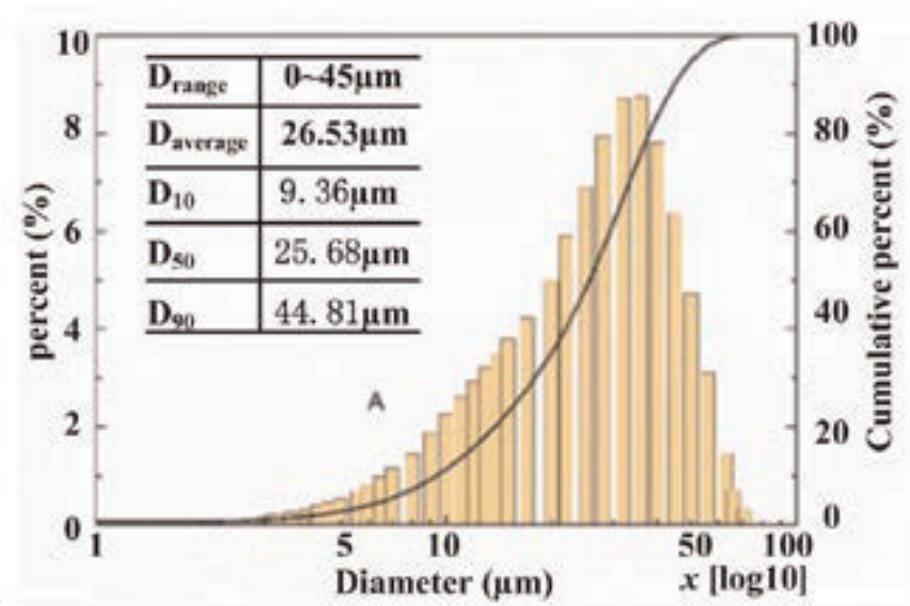
Figure 4.
(a) Microstructure of the AlSi10Mg powder, (b) the particles size distribution.
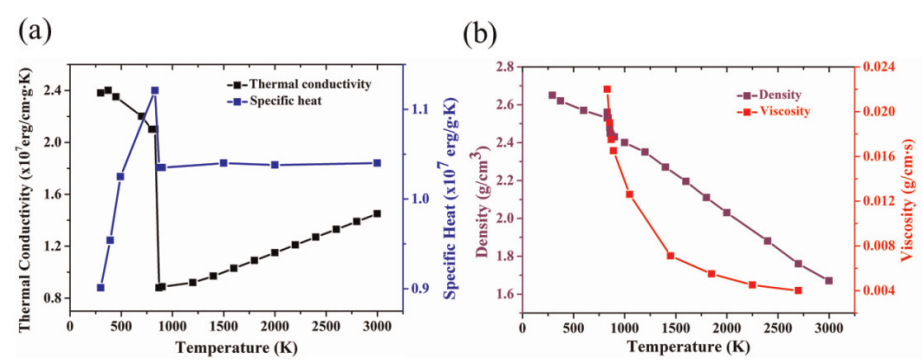

Figure 5.
Thermal material properties of AlSi10Mg: (a) thermal conductivity and specific heat, (b) density and viscosity.

Parameters	Value
Ambient temperature, T_0	293.15 K
Laser power, P	180 W
Scanning speed, v	100 cm/s
Laser beam spot size, D	70 μm
Stefan-Boltzmann constant, k_B	5.67×10^{-8} W/(m^{2}K^4)
Heat transfer coefficient, h_c	82 W/(m^{2}K)
Radiation emissivity, ε	0.4
Powder layer thickness, d	25–50 μm
Hatch spacing, H	50–70 μm
Powder size distribution	0–45 μm, Gaussian
AlSi10Mg solidus point, T_s	830.15 K
AlSi10Mg liquids point, T_l	870.15 K

Table 2.
SLM-processing conditions and material parameters used in this work.

2.3 Results and discussion

2.3.1 Model verification

Single melting track can used to validate the correction of the model and available of software. At experiment, the laser power and powder layer thickness were fixed at 180 W and 35 μm, and the laser scanning speed changed from 600 to 1600 mm. The experimental measurement criteria of the melt depth and melt width are as shown in **Figure 6a**. The melt depth is taken vertically from the free surface of the molten pool to the maximum depth of the melt boundary while the melt width is taken horizontally between the edges of the melt boundary. **Figure 6a** shows the micrograph of pool on cross section caused by Gaussian laser irradiation in the simulation and experiment for P = 180 W and v = 1000 mm/s. It is obviously that the calculated morphology of pool agree well with the experiment one. Meanwhile, **Figure 6b** shows the range and averaged experimental melt depth and width results at different laser scanning speed v with a fixed laser power P (P = 180 W,

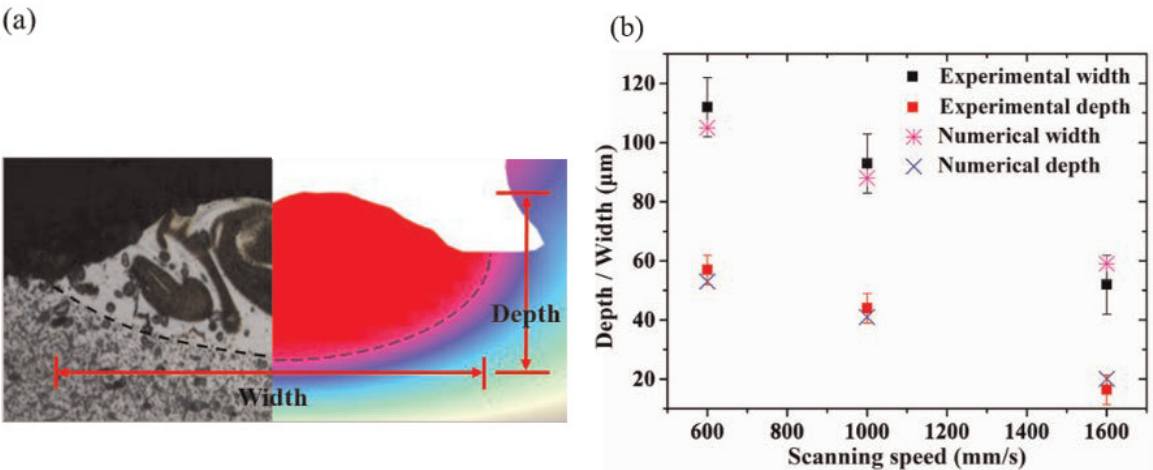**Figure 6.**
(a) Morphology of molten pool at P = 180 W and v = 1000 mm/s, (b) depth and width of molten pool at different scanning speed with a fixed P = 180 W.

v = 600, 1000, 1600 mm/s) with their corresponding simulated values. Compared the numerical depths and widths of pool with experimental results, the simulated melt depths and widths all fall within their corresponding experimental range. Due to the existence of the inherent experimental error and numerical error, the errors between experiment and simulation are inevitable. So experimental results and numerical results demonstrate the proposed numerical model can provide good predictions on shape of molten pool and, can be provided to predict the effect of layer thickness and hatching spacing on the morphology of scan track.

2.3.2 Effect of laser power and scanning speed

Figure 7 shows the powder melting and solidification evolution process in SLM. First, laser beam is turned off, as shown in **Figure 7a**. When the laser is turned on, the beam energy is absorbed by the powder layer. With the heat accumulation of powder, powder layer melts. In **Figure 7b**, a depression area is made by the work of recoil force. Because the apply of laser beam in Gaussian distribution, the temperature gradient is created between the molten pool center and the molten pool edge, with the induced surface tension gradient and the Marangoni effect. Lastly, the depression area was filled with fluid by the Marangoni effect, as shown in **Figure 7c**.

Figure 8 shows the characteristic microstructure on the polished cross section of the SLM-processed AlSi10Mg samples. The cross-section of the samples produced
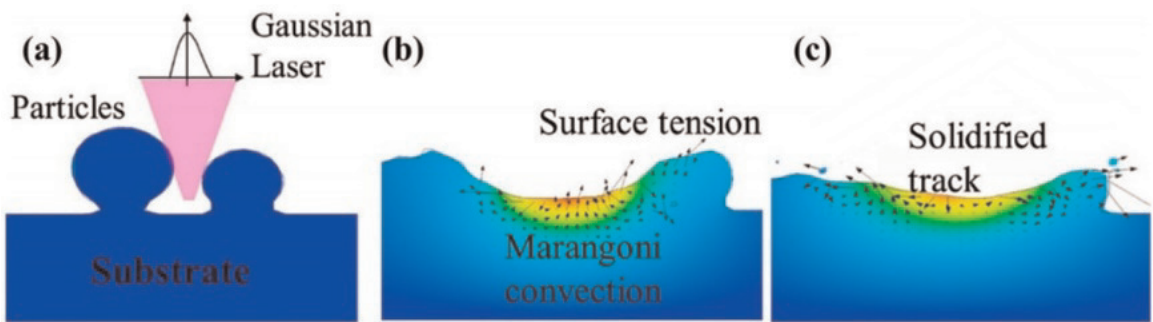

Figure 7.
Powder melting and solidification process evolution at the laser power of 180 W and scan speed of 1000 mm/s: (a) initial state (b) heating process (c) solidification.
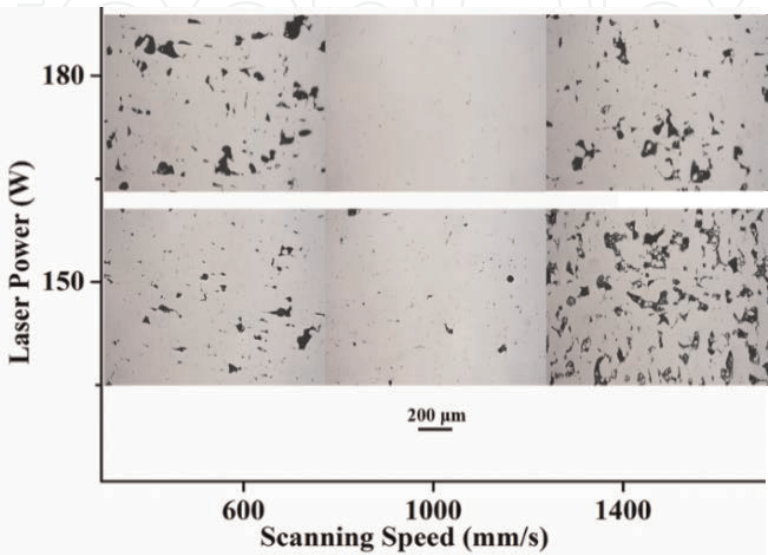

Figure 8.
Influence of laser power and scanning speed on the microstructure of SLM-processed samples.

by using the laser power of 180 W and scan speed of 1000 mm/s showed a fine microstructure without any apparent pores. At the low laser power of 150 W or scan speed of 600 mm/s, the cross-section of the as-built samples consisted of irregular-shaped pores were visible. However, at relatively high laser scan speed of 1400 mm/s, a large amount of the balling formation was present on the cross-section. It can be concluded that the balling phenomena was one of the typical metallurgical defects at high laser scan speed. In order to understand how the laser power P combined with the laser scan speed v affects the pores and balling defects, the line energy density (LED) is defined as [24]:

$$LED = \frac{P}{v} \tag{11}$$

Furthermore, the numerical studies were used to describe the forming mechanism of the metallurgical defects during laser melting and to provide a basis for the process optimization. The laser melting process of the AlSi10Mg powder at different scan times was shown in **Figure 9a**. In order to assess the effect of the LED on heating of the powder, the peak temperature and the interfacial velocity at the edge of the molten pool was rescored as the center of the laser beam moved to the point of $X = 0.36$ mm and $Y = 0.1$ mm. As shown in **Figure 9b**, the peak temperature and the interfacial velocity increased from 1810 K and 1.2 m/s to 2831 K and 5.1 m/s as the applied LED increased from 1.071 to 3 J/cm, respectively. At a relatively low LED, the insufficient laser energy result in insufficient melting of the powder. As
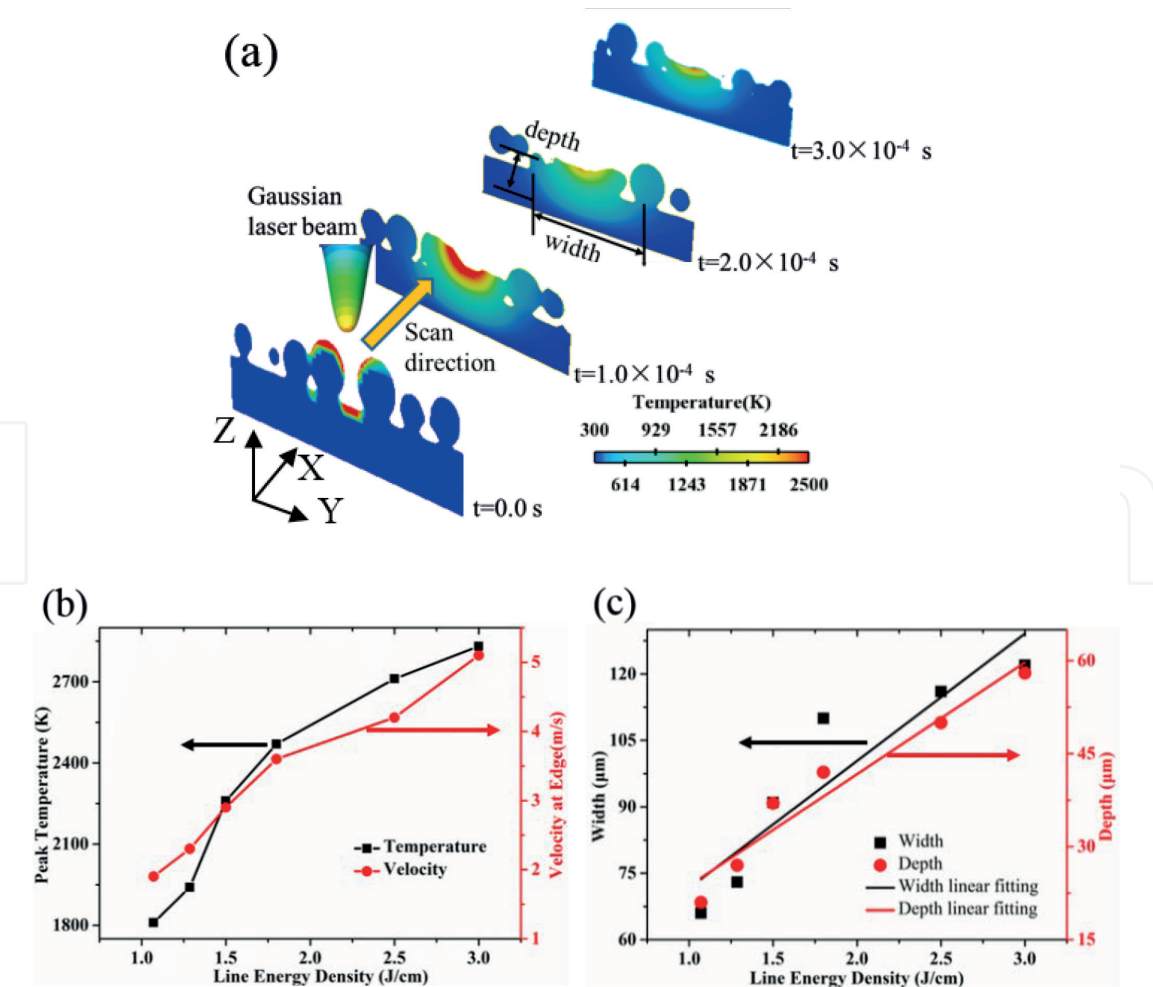

Figure 9.
(a) Temperature field and surface melt velocity obtained by simulation at condition of P = 180 W and v = 1000 mm/s. (b) Influence of line energy density on the peak temperature and surface melt velocity of molten pool. (c) Influence of line energy density on the width and depth of molten pool.

shown in **Figure 9c**, the depth of the molten pool is about 20 μm at LED of 1.071 J/cm. This implies that the low applied LED can lead to the insufficient melting of the powder and the resultant interlayer pores. In addition, the balling phenomena was severely occurred in this condition. On the contrary, at relatively high LED, the high temperature of the molten pool leads to a strong perturbation within the molten pool, thereby resulting in the instability of the free surface of the molten pool. In this case, a large amount of the pores was generated by the instability of the scan track [24].

When the laser moves to the point of X = 0.36 mm along scanning direction, the molten pool was chosen in this case.

2.3.3 Effect of hatching spacing

Figure 10 shows that at an interconnect pores will be formed in the overlap if the large interconnected gap has not been completely filled by re-melting liquid because of the high hatching spacing. An overlap in the multi-tracks is necessary to have continuity between two adjacent scan tracks leading to a dense solidification. Due to the overlap between the successive adjacent scans, the hatching spacing is always less than the laser beam radius. Hatch spacing is another parameter, which is highly affects the pore formation.

As revealed in **Figure 11**, at laser power of 180 W and scan speed of 1000 mm/s, the number of the inter-track pores was apparently reduced as the hatch spacing
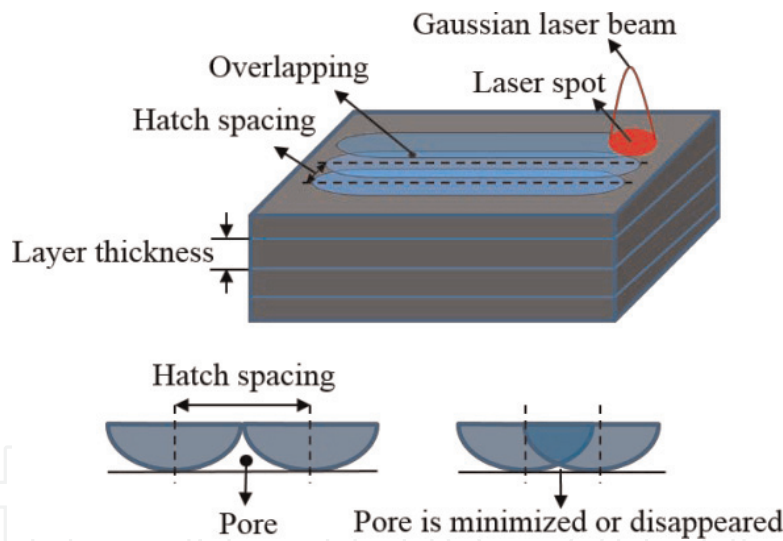
Figure 10.
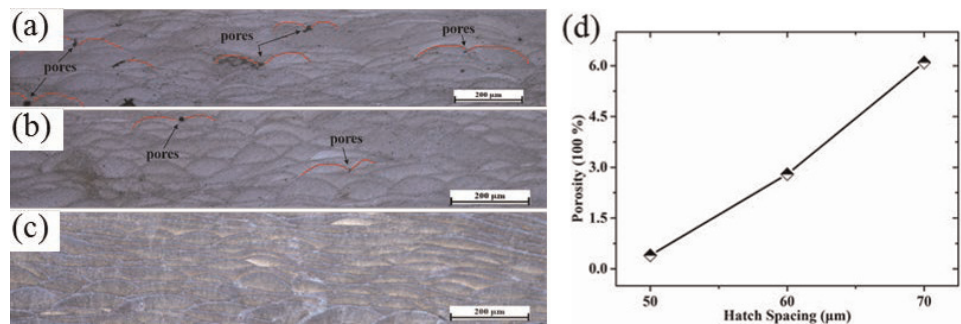*The effect of hatching spacing on the formation of porosity in overlap between adjacent scan tracks.*

Figure 11.
Typical microstructure of the SLM-processed AlSi10Mg samples at hatch spacing of (a) 70 μm, (b) 60 μm, and (c) 50 μm. (d) Effect of the hatch spacing on the porosity of the as-built sample. The laser power of P = 180 W, scan speed of v = 1000 mm/s and layer thickness of d = 35 μm were fixed in these experiments.

decreased from 70 to 50 µm. As a result, the porosity of the SLM-processed sample was accordingly reduced from 6.1 to 0.3% (**Figure 11d**). Since at a relatively larger hatch spacing, the portion of the re-melted material was reduced, leading to insufficient overlap between two adjacent scan tracks.

As the case in **Figure 12**, the insufficient overlap will increase the possibility of the inter-track pores formation. In general, reducing the hatch spacing is beneficial for the reduction of the inter-track pores [3]. However, as the relatively low hatch spacing applied during SLM, although a fine bonding between two adjacent scan tracks can be obtained, the build efficiency was decreased under this condition. So it is important to choose a reasonable hatch spacing during SLM.

2.3.4 Effect of layer thickness

The powder layer thickness is one of the important factors in in producing the pores formation. **Figure 13** shows the topography of the second scan track formed by SLM using different powder layer thickness. It is clearly that a relatively continuous and stable scan track was generated at powder layer thickness of 35 µm. At low layer thickness of 25 µm or larger layer thickness of 50 µm, the scan track showed a severe irregular profile which will increase the possibility of the inter-layer pore
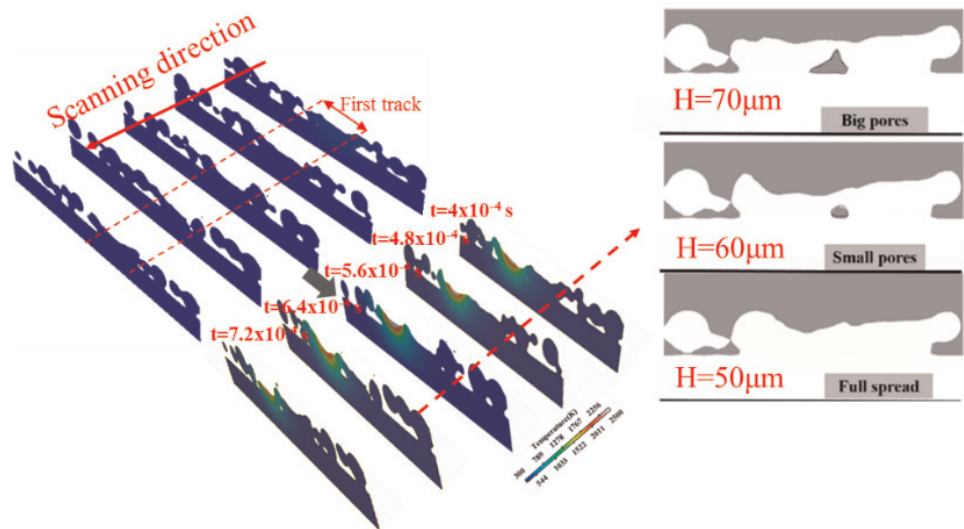

Figure 12.
Bonding between two adjacent tracks at laser power P = 180 W, scan speed v = 1000 mm/s, and hatch spacing of 50, 60, 70 µm.
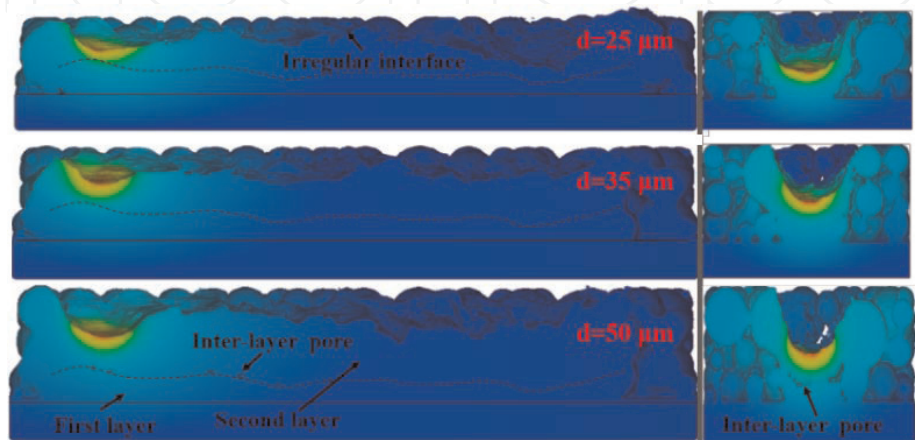

Figure 13.
Influence of powder layer thickness on morphology of scan track in longitudinal view (left) and cross-sectional view (right). Laser power P = 180 W and scanning speed v = 1000 mm/s were fixed in simulations.
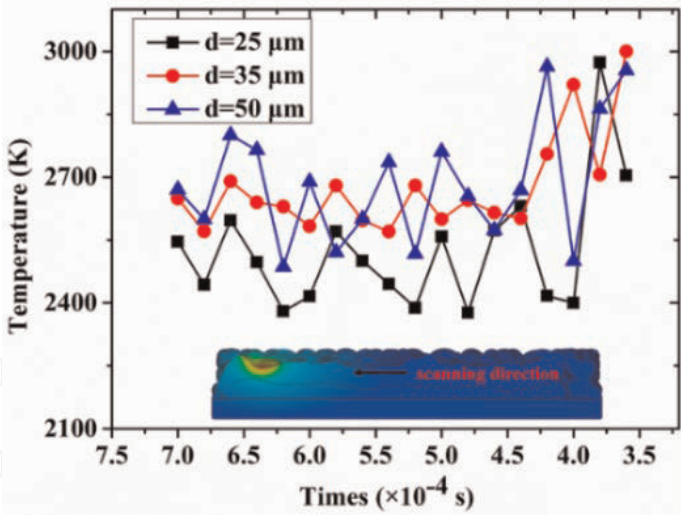
Figure 14.
Influence of powder layer thickness on the temperature of molten pool. Laser power P = 180 W and scanning speed v = 1000 mm/s were fixed in simulations.

formation. This is due to as the relatively larger powder layer thickness applied during SLM, the laser energy cannot melt previous layer, inducing inter-layer pores in the interface between two adjacent layers. However, decreasing the powder layer thickness increase the reflected radiation from the surface of the previous track, hence decreasing the peak temperature of molten pool, as shown in **Figure 14**. At powder layer thickness of 25 μm, the peak temperature of molten pool exhibits apparent fluctuation, and the following will produce the scan track with irregular surface. According to this numerical result, the thin powder layer thickness of 35 μm is recommended for AlSi10Mg in SLM process.

The pore and the balling defects lead to a decrease in the densification level of the SLM-processed samples. To evaluate the combined effect of the laser power P, scan speed v, hatch spacing H, and powder layer thickness d on the densification level of the as-built samples, a volumetric energy density (VED) is defined as:

$$VED = \frac{P}{vHd} \tag{12}$$

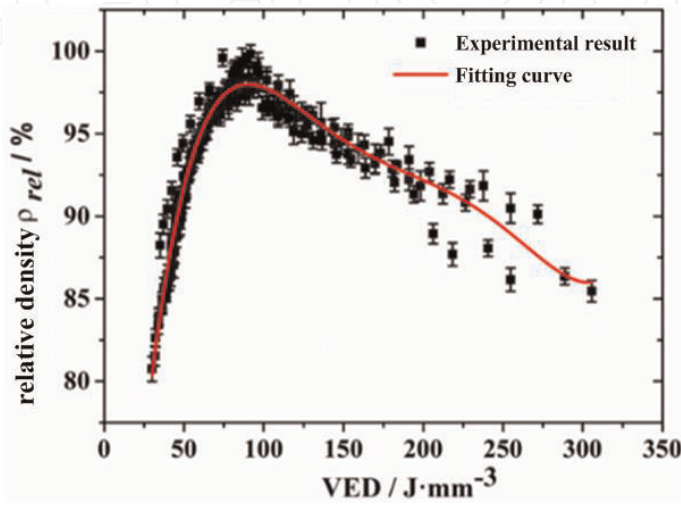The relative density of the SLM-processed AlSi10Mg sample are shown in **Figure 15** as a function of the VED.

Figure 15.
Effect of the VED on the relative density of the SLM-processed samples.

As the applied VED within the range of 75–105 J/mm^3 during laser melting, the relative density of the as-built samples is larger than 97.5%. According to all the above research results, the VED of 102.86 J/mm^3 (P = 180 W, v = 1000 mm/s, H = 50 μm, d = 35 μm) was proposed during AlSi10Mg SLM process.

3. Numerical investigation of thermocapillary-induced deposited shape in MFCAM of aluminum alloy

A three-dimensional (3D) numerical model with volume of fluid method is developed for metal fused-coating additive manufacturing (MFCAM) process of aluminum (Al) alloys. It predicts the thermal flow field in the thermocapillary-induced melt, the surface deformation and solidified deposition geometry during MFCAM in successive depositing passes. Verification of the numerical model was performed by comparing the calculated results with metallography of deposited cross-sections, showing that there is a good qualitative agreement between the two, which indicates that the established numerical model is capable of simulating the complex heat and mass transfer phenomena in the varying polarity gas tungsten arc welding (VP-GTAW) based additive manufacturing. The effects of melt flow rate and the gap height between the substrate and fused-coating head on deposition geometry were studied. The results show that the deposition geometry is closely correlated to the melt flow rate. Increase in melt flow rate will lead to the obvious increase of deposition height, but the reverse is true in the gap height. These detailed physical insights facilitate the prediction of deposition defects in MFCAM of aluminum alloy.

3.1 Principle of MFCAM process

The schematic illustration of MFCAM process is shown in **Figure 16**. The experimental system is mainly composed of an induction heating, gas protection device, a pressure controller and a movable platform. The deposits of aluminum alloy can be created following the layer-by-layer approach by controlling the synchronization of the movable platform and the extrusion of liquid metal. A programmable multi-axis controller (PMAC) can be used to control the motion of
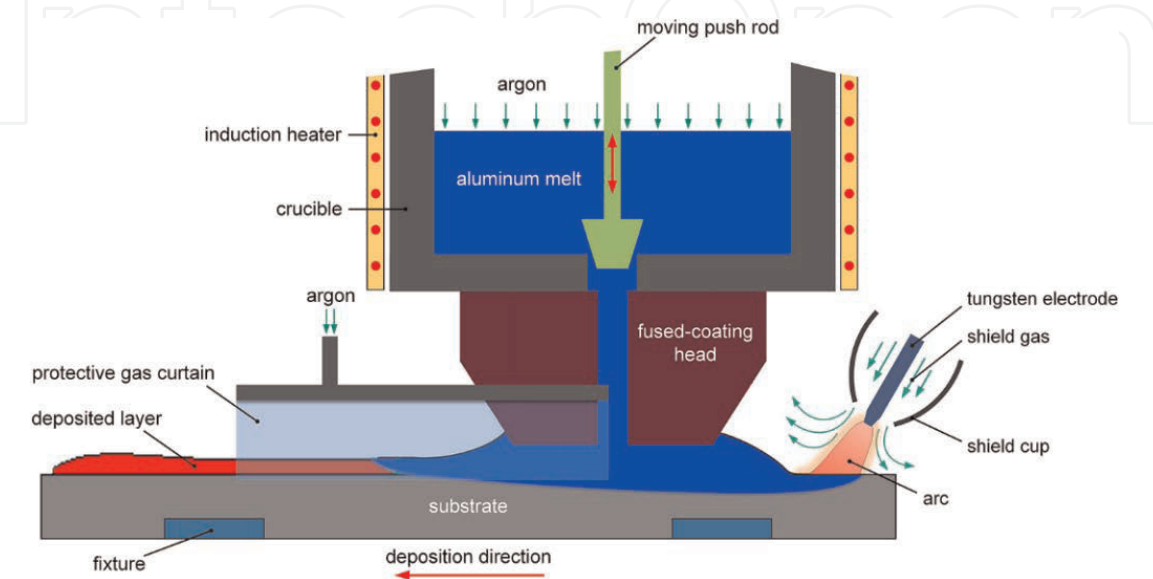

Figure 16.
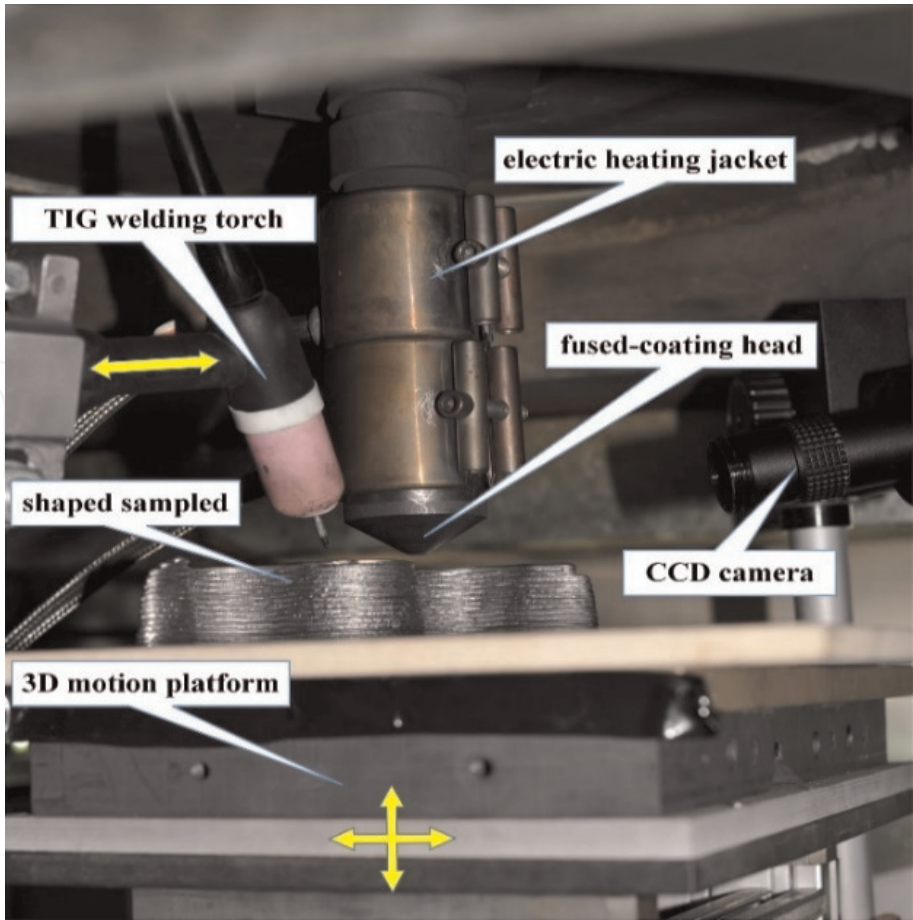*Schematic diagram of MFCAM process.*

Figure 17.
Experimental setup for the MFCAM of Al alloys.

movable platform. The high-temperature liquid metal would flow through the inner flow channel of fused-coating head under the combined-action of moving push rod, surface tension and hydrostatic pressure. As the liquid metal contacts with the substrate surface or the previously deposited layers, a local thermocapillary-induced flow region will be created rapidly. To achieve a metallurgical bonding between the deposited layers, a pulsed variable polarity GTA welding arc was adopted to create a shallow molten pool in front of the thermocapillary-induced flow region. On the other hand, variable polarity GTAW arc can timely remove the aluminum oxide on the deposits. Last but not least, the local solidification conditions and thermocapillary-driven spreading motion of the melt can be tunable by arc heat input and the relative distance between welding arc and fused-coating head.

The corresponding experimental setup for the MFCAM of Al alloys is shown in **Figure 17**.

3.2 Materials and methods

3.2.1 Experimental procedure

The base material was 2024 aluminum alloy in initial T6 condition with a thickness of 6 mm. The material was cut into several pieces with $300 \times 60 \times 6 \text{ mm}^3$ dimensions. The nominal chemical composition of the base metal is shown in **Table 3**. Pure argon (99%) was employed as shielding gas with flow rates of 15–18 L/min for VP-GTAW.

Cu	Si	Mn	Mg	Zn	Ti	Al
4.52	0.16	0.61	1.4	0.08	0.05	Remain

Table 3.
Chemical composition of the deposited 2024 aluminum alloy/wt%.

In VP-GTAW welding system, Fronius MagicWave 3000 welding power source was adopted. The VP-GTA welding process was used square wave AC mode. Before deposition, oil and other impurities were removed using acetone. The arc welding parameters applied in the experiments are presented in **Table 4**. Among them, the magnitude of DCEN welding current is I_{en}, the magnitude of DCEP welding current is I_{ep}, the welding speed is u, the pulse frequency is f. The DCEP duty ratio of VP arc was fixed at 50%.

After the experiments, the samples for metallographic observations were prepared by sectioning the deposits along the vertical direction using an electrical discharge wire cutting machine (Suzhou Simos CNC Technology Co., Ltd., Suzhou, China). Then, the samples were etched with modified Keller solution (50 ml H_2O, 1 ml HCL, 1.5 ml HF, and 2.5 ml HNO_3) after the processes of rough grinding, fine grinding, and polishing. The microstructure of the treated specimen was observed by Eclipse MA200 light microscope (OM) (Nikon Instruments (Shanghai) Co., Ltd., Shanghai, China).

3.2.2 Numerical modeling of MFCAM process

3.2.2.1 Physical model assumptions

A numerical model coupling electromagnetism force, heat transfer, and fluid flow in melt is derived in this section. The electric arc is modeled by an equivalent heat source applied to the upper surface of a workpiece. Gaussian distribution function can be used to describe the modeled electric arc quantities. It was assumed that the welding torch moves at a constant welding speed. The electromagnetic, continuity, momentum, and energy equations can be solved in the weld pool. The considered problem possesses symmetry with respect to the longitudinal vertical median plane, can therefore be calculated as one-half plate.

Up to now, there is no direct literature addressing the quantitative relation of shielding gas flow rate and weld bead dimensions during the VP-GTAW process. There is an optimum flow rate for weld shielding gases, but this is often decided by preference or experience. In this study, the thermocapillary-driven flow region is protected from atmosphere by pure argon (Ar) gas, and the flowing rate of the shielding gas was 15–18 L/min.

Test case	Adjustable parameters		Other fixed parameters
	f (Hz)	u (mm/s)	
T1	5	4	I_{en}/I_{ep} = 240/120 A
T2	5	5	U_{en}/U_{ep} = 12.0/11.2 V $\sigma_{j,\ EN}/\sigma_{j,\ EP}$ = 2.70/2.62 mm $\sigma_{q,\ EN}/\sigma_{q,\ EP}$ = 2.70/2.62 mm
T3	5	6	$\sigma_{p,\ EN}/\sigma_{p,\ EP}$ = 3.00/2.92 mm η_{en}/η_{ep} = 0.8/0.5

Table 4.
Parameters for VP-GTA welding of aluminum.

3.2.2.2 Governing equations

The numerical simulation of heat and mass transfer processes are governed by a set of equations in Flow3D model. In the present study, the liquid metal is assumed to be incompressible Newtonian fluid, and the flow should be laminar. The electric arc was assumed as an internal boundary condition can be described as Eq. (13).

$$k\frac{\partial T}{\partial \vec{n}} = \dot{q}_{arc} - \dot{q}_{conv} - \dot{q}_{rad} \tag{13}$$

where q_{arc}, q_{conv}, q_{rad} are the arc heat input, convective and radiative heat loss, respectively, $\vec{n}$ is the surface normal.

In this study, according to the actual processing conditions that the welding current in case of DCEP and DCEN (I_{en}/I_{ep} = 240/120 A) is high enough, arc stiffness and impact force exerted onto the weld pool surface is larger, and the arc column is perpendicular to the surface of the weldment. So, the Goldak's double-ellipsoidal heat source model was adopted [25], which can provide relatively accurate results, especially for the low penetration surface melting process. In the moving volumetric heat source model, the power density distributions of the front and rear quadrants can be described by Eqs. (14) and (15), respectively,

$$q_r = \frac{6\sqrt{3}q_{arc}f_r}{\pi a_r bc\sqrt{\pi}} \exp\left(-3[\frac{x^2}{a_r^2}+\frac{y^2}{b^2}+\frac{z^2}{c^2}]\right) \tag{14}$$

$$q_f = \frac{6\sqrt{3}q_{arc}f_f}{\pi a_f bc\sqrt{\pi}} \exp\left(-3[\frac{x^2}{a_f^2}+\frac{y^2}{b^2}+\frac{z^2}{c^2}]\right) \tag{15}$$

where f_f and f_r are the front and rear fraction of the heat flux; a_f, a_r, b and c are the parametric values obtained from the metallographic data and the weld bead profile; q_{arc} is the welding arc heat input.

The heat loss $\dot{q}_{conv}$ and $\dot{q}_{rad}$ can be calculated as follow:

$$\dot{q}_{conv} = h_{conv}(T - T_0) \tag{16}$$

$$\dot{q}_{rad} = \varepsilon\sigma_{sb}(T^4 - T_0^4) \tag{17}$$

According to the Vinokurov's empirical model [26], combined convection-radiation heat transfer coefficient was utilized as:

$$h_{vino} = 2.41 \times 10^{-3}\varepsilon T^{1.61} \tag{18}$$

The pressure boundary conditions on the weld pool surface can be described as Eq. (19).

$$P = P_{arc} + \frac{\gamma}{R_c} \tag{19}$$

where P_{arc} is the arc pressure, R_c is the curvature radius of the weld pool surface. The surface tension γ can be calculated as follow:

$$\gamma = \gamma_0 - \gamma_T (T - T_l) \tag{20}$$

The arc pressure distribution was assumed to follow the distribution of current density. It can be modeled by a Gaussian model with the same radius of arc drag force, as blow [27].

$$P_{arc}(x, y) = \frac{\mu_0 I^2}{4\pi^2 \sigma_r^2} \exp\left(-\left(\frac{r^2}{2\sigma_r^2}\right)\right) \tag{21}$$

where μ_0 is the magnetic permeability of free space, σ_r is the arc pressure parameter (DCEN phase: $\sigma_r = \sigma_{p, EN}$; DCEP phase: $\sigma_r = \sigma_{p, EP}$).

The arc drag force on the weld pool is greatly dependent on the current, the composition of shielding gas, and the tip angle of electrode. Here, the effect of arc drag force is considered as a spatial boundary distribution, which can be represented as follows [28].

$$P_{Drag}(r) = P_{Max} \sqrt{\frac{r}{r_{Shear}}} \exp - (\frac{r}{r_{Shear}})^2 \tag{22}$$

where r_{Shear} is the distribution parameter of arc drag force.

The body force mainly includes electromagnetic force (EMF), gravity, and buoyancy. The gravity acceleration is 9.81 m/s². The temperature-dependent properties were used for the density. The electromagnetic force, as an important body force, was considered by adopting the elliptically symmetric welding current density [29, 30]. The equations relating EMF are listed as below.

$$F_x = -J_z \times B_\theta \frac{x}{r_a} \tag{23}$$

$$F_z = -J_r \times B_\theta \tag{24}$$

$$J_z = \frac{I}{2\pi} \int_0^\infty \lambda J_0(\lambda r_a) \exp\left(-\frac{\lambda^2 \sigma_x}{2}\right) \frac{\sinh[\lambda(c-z)]}{\sinh(\lambda c)} d\lambda \tag{25}$$

$$J_r = \frac{I}{2\pi} \int_0^\infty \lambda J_1(\lambda r_a) \exp\left(-\frac{\lambda^2 \sigma_x}{2}\right) \frac{\cosh[\lambda(c-z)]}{\sinh(\lambda c)} d\lambda \tag{26}$$

$$B_\theta = \frac{\mu_m I}{2\pi} \int_0^\infty J_1(\lambda r_a) \exp\left(-\frac{\lambda^2 \sigma_x}{2}\right) \frac{\sinh[\lambda(c-z)]}{\sinh(\lambda c)} d\lambda \tag{27}$$

$$r_a = \sqrt{(x - x_0)^2 + [\frac{\sigma_x}{\sigma_y}(y - y_0)]^2} \tag{28}$$

where I is the arc current (DCEN phase: $I = I_{en}$, $\sigma_j = \sigma_{j, EN}$; DCEP phase: $I = I_{ep}$, $\sigma_j = \sigma_{j, EP}$), F_i are the components of the EMF force in the i-direction ($i = x, y, z$), B_θ is the angular component of the magnetic field, J_z and J_r are the axial and radial

current density in the cylindrical coordinate system, J_0 and J_1 are the zero order and one order Bessel function, respectively, z indicates the vertical depth from top surface of workpiece, and c is the workpiece thickness.

3.2.2.3 Numerical model

A 2D longitudinal section of the 3D calculation model for MFCAM process is shown in **Figure 18**. The structural parameters of the model are: d is 1.2 mm, D is 4 mm; h is 1.2–2.4 mm; the substrate thickness is 6 mm, and the distance from arc to the rim of coating head is ∼5.5 mm.

In the present study, peak current I_p (voltage) and base current I_b (voltage) are 220 A (18.2 V) and 183 A (16.7 V), respectively. The proportion of peak current time in one cycle is 0.5. Thermo-physical properties of material used in this study are listed in **Table 5**. The contact angle, defined as the angle at which the liquid metal meets the workpiece surface, is assumed to be 90°.

A grid size (200 μm) and computational time-step (2.5×10^{-6} s) for simulations are used. It took ∼72 h to run 6 s of real-time simulation of a single-track deposition using high-performance computer of 48×1.6 GHz CPU.

3.3 Results and discussion

3.3.1 Experimental verification of the numerical model

To confirm the predictive accuracy of the established model, the corresponding deposition experiments were carried out. A cathode with 60° cone angle and a 3.2 mm radius float tip provides a good combination. The distance between tungsten electrode tip and workpiece surface was fixed at 4 mm. To avoid heat sinks, the workpieces need to be thermally insulated from the fixtures in VP-GTA welding process. Verifications of the numerical model were carried out by comparing the calculated results with the metallographic macro-sections. **Figure 19** presents the simulated and measured geometry of a single-track deposition by MFACM.

Calculated solidus isotherm 811 K—corresponds to the fusion line obtained in the experiments. It is found that the calculated deposition geometries and dimensions agree well with the experimental data. The average values of deposition width and penetration depth were measured to be 8.65 and 1.43 mm, respectively, which is in consistent with the calculated results. The average relative errors of the deposition width and height are never exceeded 5.7 and 11.5%. The fidelity of the models will be verified to better predict the surface evolution in MFCAM process and eliminate the deposition defects based on the understanding of its mechanism.
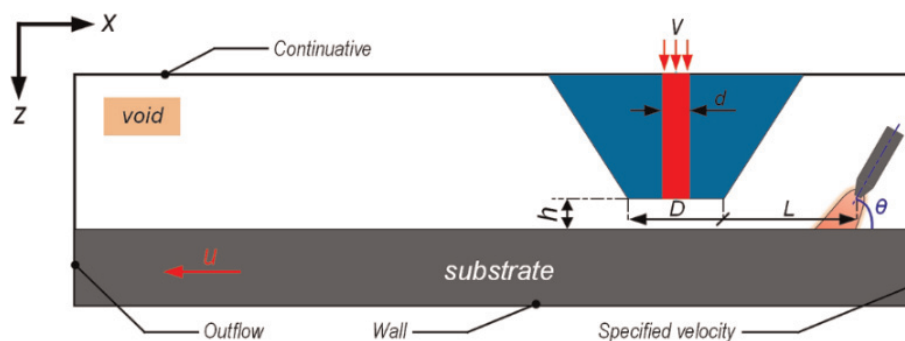

Figure 18.
Calculation model for FCAM process.

Nomenclature	Value
Density (kg m^{-3})	$f(T)$ [21]
Viscosity (N s/m^2)	$f(T)$ [21]
Surface tension (N m^{-1})	$f(T)$ [21]
Thermal conductivity (W m^{-1} K^{-1})	$f(T)$ [21]
Specific heat (J kg^{-1} K^{-1})	$f(T)$ [21]
Solidus temperature (K)	$T_s = 811$
Liquidus temperature (K)	$T_l = 905$
Latent heat for melting (J kg^{-1})	$h_{sl} = 3.97 \times 10^5$
Coefficient of thermal expansion (K^{-1})	$\beta = 1.5 \times 10^{-4}$
Radiation emissivity	$\varepsilon = 0.4$
Initial temperature of melt (K)	960
Substrate temperature (K)	298
Volume flow rate of the melt (mm^3 s^{-1})	$V = 30$–70
Substrate moving speed (mm s^{-1})	$U = 3$–9
Ambient temperature (K)	$T_\infty = 300$
Vaporization temperature (K)	$T_{ev} = 1163$
Arc thermal efficiency	$\eta = 0.7$ [22]
Distribution parameter of arc drag force (mm)	3.2

Table 5.
Thermo-physical material properties of 2024 aluminum alloy and calculation data used in the simulation.
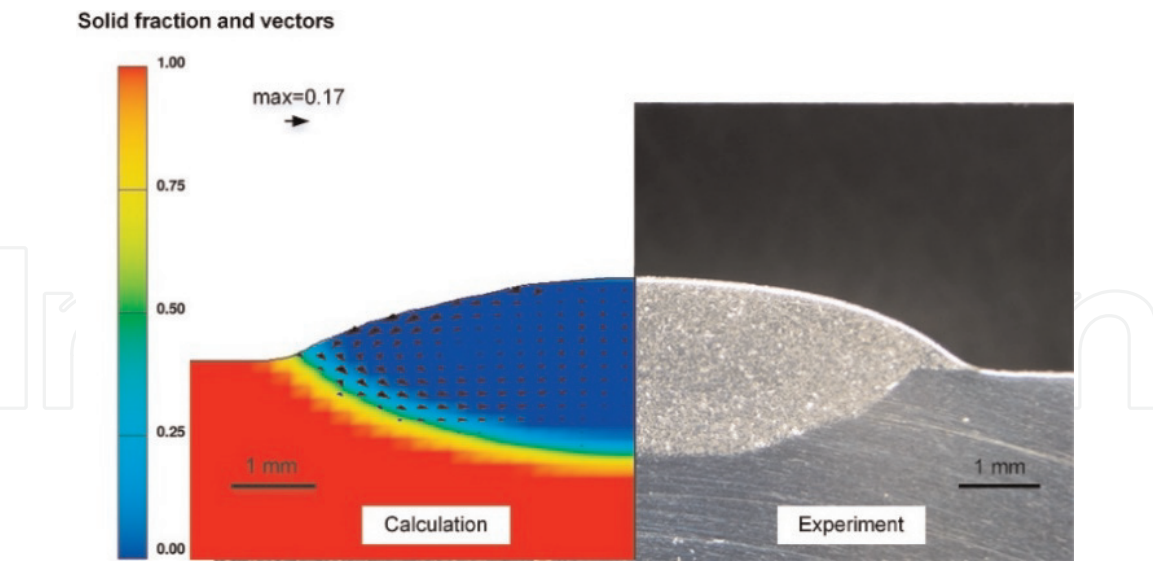

Figure 19.
Comparison between computed thermal profile (left) and experimentally determined (right) cross-section of a single-track deposition, all dimensions are in mm.

3.3.2 Thermophysical phenomena in MFCAM

During the fused-coating deposition process, the zone where the heat source is characterized by the temperature local sharp increase and being heated up to the state of melting, as shown in **Figure 20**. We need to how this evolutionary sequence of deposited layers. The development of deposition shape and the heat transfer and
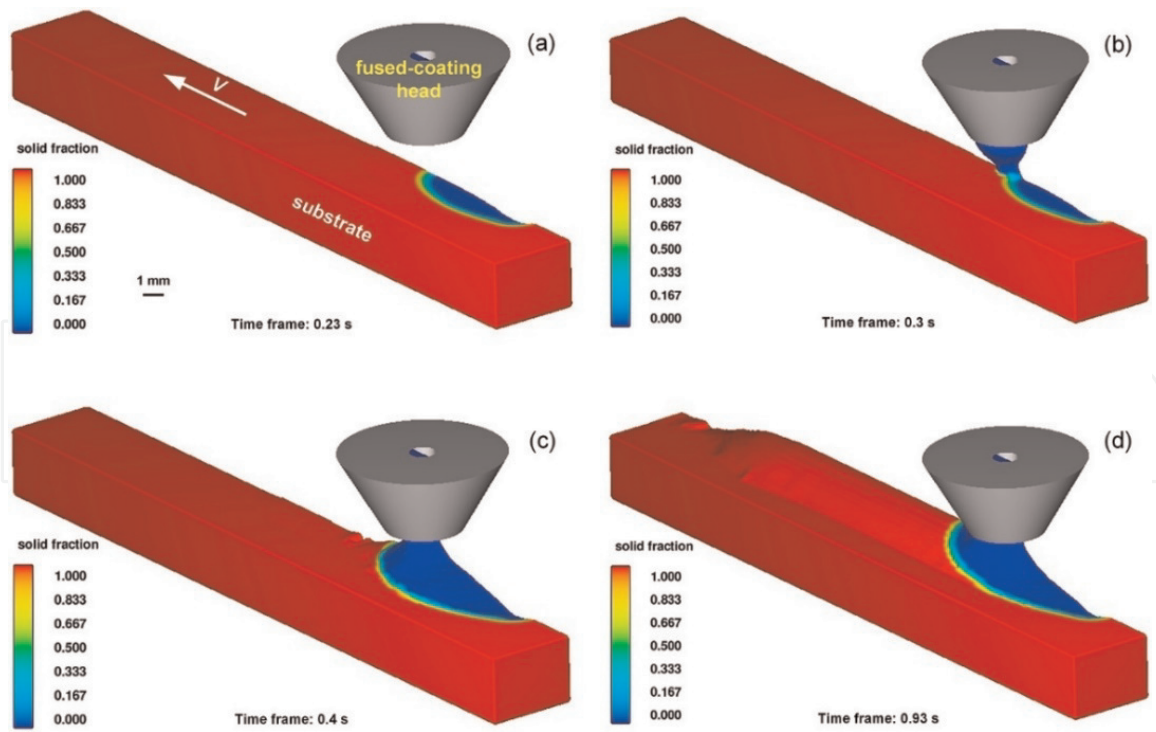
Figure 20.
Solid fraction distribution and the changes of surface morphology of the melt in four stages during single-track deposition. (a) formation of a shallow molten pool, (b) extrusion process of the melt, (c) extremely changes of surface morphology of the melt, and (d) relatively steady state.

flow characteristics of liquid metal were illustrated. The shape evolution of each single layer can be divided into four stages: (i) formation and growth of a shallow molten pool, (ii) extrusion process of the melt, (iii) extremely changes of surface morphology of the melt, and (iv) relatively steady state.

The shallow molten pool on a moving metal substrate is firstly created in the initial stage. The source of heat in welding is enough to melt the metal. According to the practical conditions, the welding torch needs to be tilted from the nominal center of the workpiece surface, which will slightly change the thermal flow field characteristics of the molten pool.

During the second stage of MFCAM process the hot liquid Al alloy will be extruded continuously toward the shallow molten pool. Meanwhile, the heat flux of the tilted welding arc still melts the base metal. Thus, the local thermal contact resistance of deposition regions can be reduced greatly, which is beneficial to the spreading of the melt. The corresponding thermal and flow fields in this stage is shown in **Figure 21**.

In the third stage, the extruded liquid alloy and the melt in the shallow molten pool trend to spontaneous fusion once the extruded liquid metal meets the surface of the molten pool. The free surface of the melt will experience extremely complex deformations. **Figure 22** illustrates the topology changes in the free surface, surface depression in the molten pool and the temperature distributions in the melt.

It can be seen from **Figure 22a** that there is a higher temperature region between the welding arc and fused-coating head. The teardrop-shaped gouging region is also found in the front of the molten pool. The causes of these phenomena can be attributed to the fact that it is relative difficult for the liquid metal located in the higher temperature region to dissipate heat because of the heat input by welding arc, at the same time, the melt continuously obtains latent heat from the being extruded liquid metal. The end-face of the coating head and the shallow molten pool will produce an obviously restriction effect to the spreading melt. As shown in **Figure 22b**, the local fluctuations of the melt's surface and solidification front are
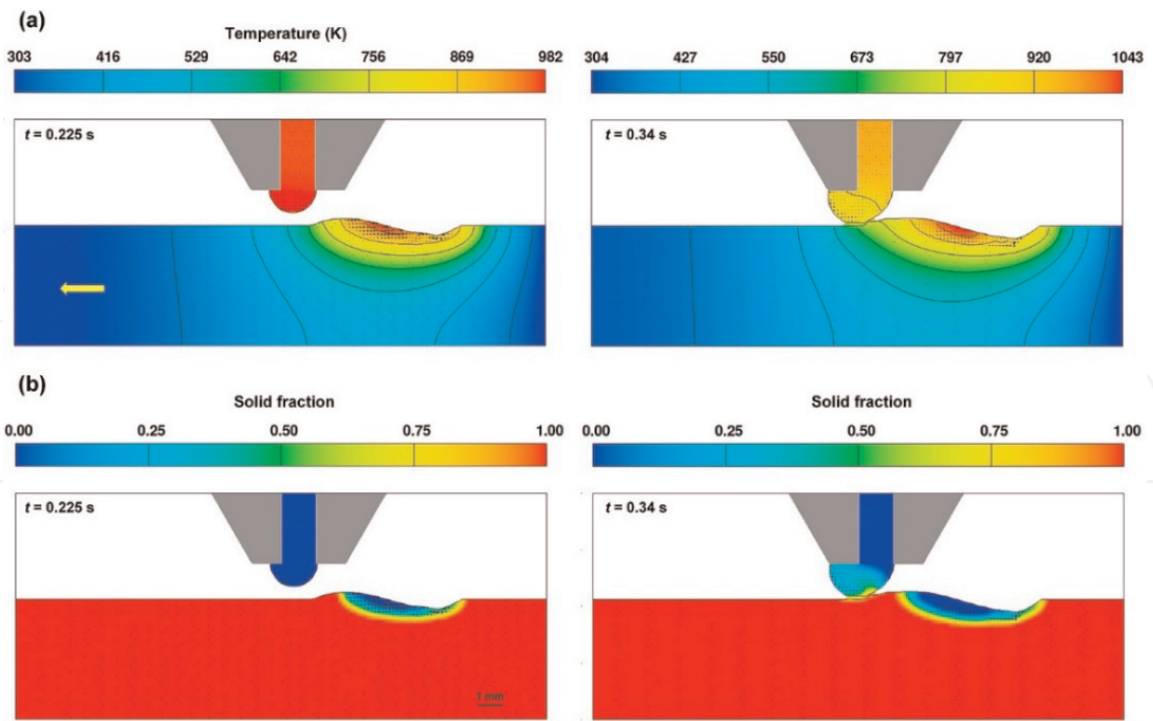
Figure 21.
Side views of (a) temperature distributions, and (b) solid fraction distributions in the second stage.
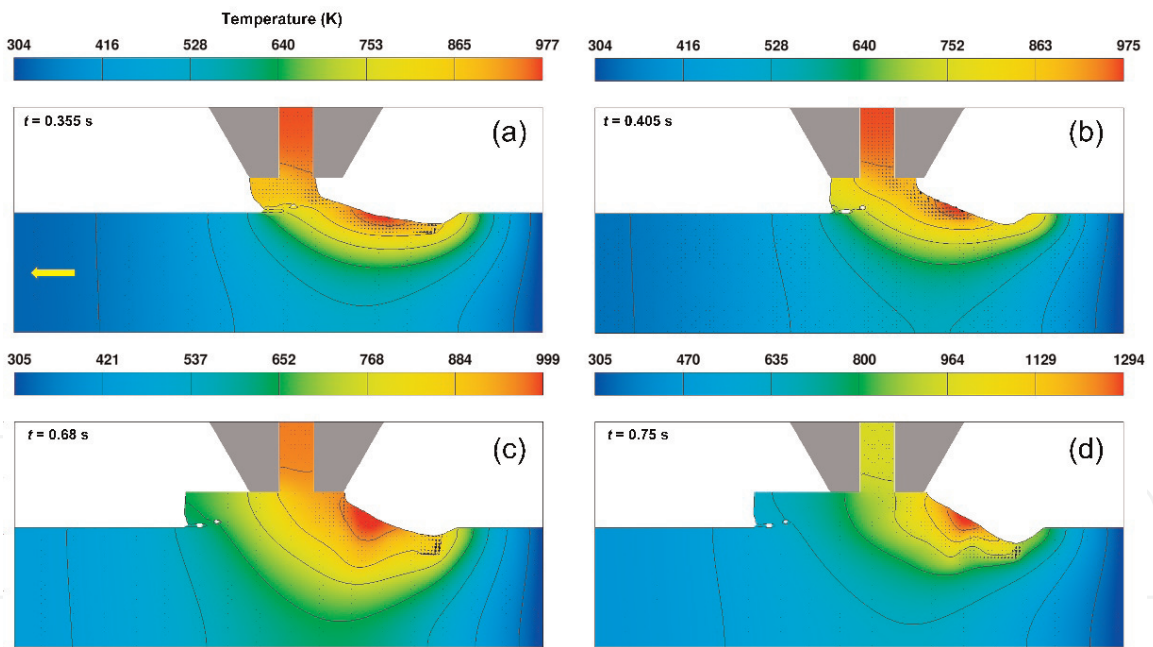

Figure 22.
Topology changes in the free surface, surface depression in the molten pool and the temperature distributions in the melt. (a) t = 0.355 s, (b) 0.405 s, (c) 0.68 s, and (d) 0.75 s.

always found, this could be attributed to the way in which a pulsed-current mode was adopted.

As time goes on, the various forces governing the fluctuation of molten pool surface and a macroscopic heat balance tend to equilibrium, therefore, the thermocapillary-driven deposited shape becomes to be continuous and stable, the 3D shape of the stable deposited layer can be observed in **Figure 23**. The calculated temperature field and velocity magnitude could be illustrated by **Figure 23a**. The dimensions associated to the solidified deposited layers will be characterized by H and W.
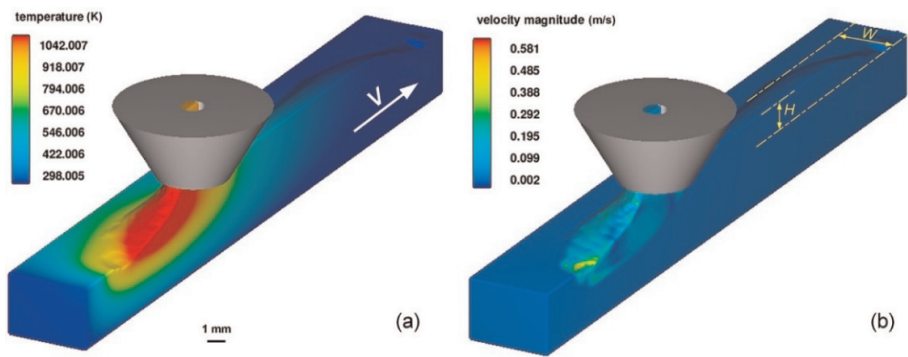
Figure 23.
(a) 3D shape of a single-track deposited layer and (b) surface velocity contour.

The calculated results show that the shape of deposited layers is flat and regular from the global aspect although there is a local fluctuation of melt's surface and solidification front. It is also found that a maximum liquid metal speed with 0.6 m/s is obtained near the center of the shallow molten pool.

3.3.3 Influence of melt flow rate

Figure 24 shows the influence of melt flow rate on the morphology characteristics of single-track deposits. The gap between substrate and fused-coating head is fixed at 1.8 mm, and the substrate moving speed is 6 mm/s.

As illustrated from **Figure 24**, an approximate linear increase in the deposition height was observed as the melt flow rate increase from 20 to 120 ml/min. However, in the respects of the deposition width, there obviously exist many highly nonlinear relationships. Therefore, the formation mechanism based on the thermal flow dynamics needs to be recognized. The principle of minimum enthalpy may be utilized to explain this phenomenon. The principle is described as follows: the thermocapillary-driven flow always has a characteristic to keep the minimum enthalpy value by automatically changing its size and adjusting its enthalpy. In
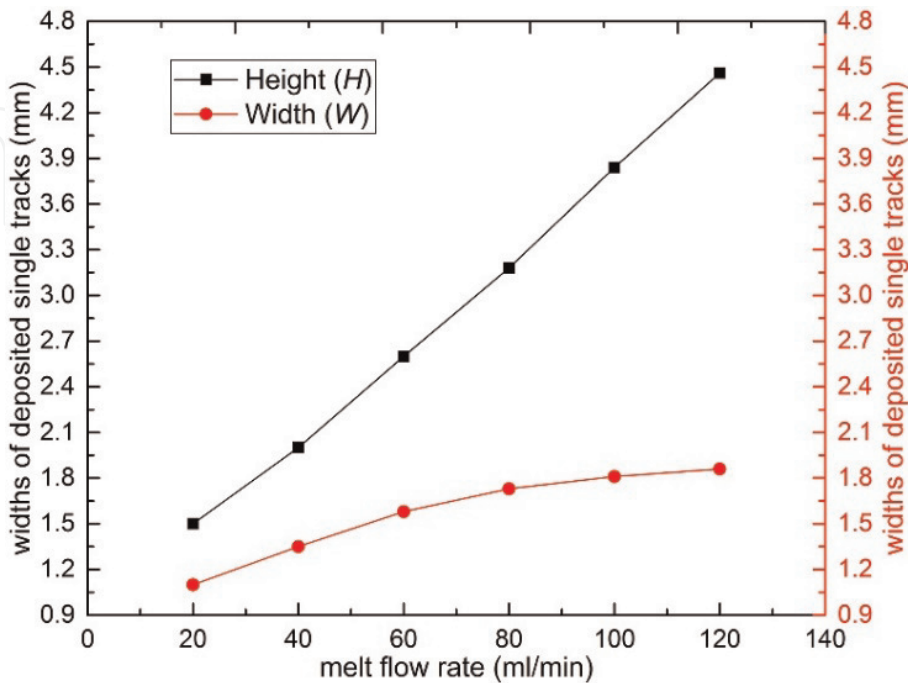

Figure 24.
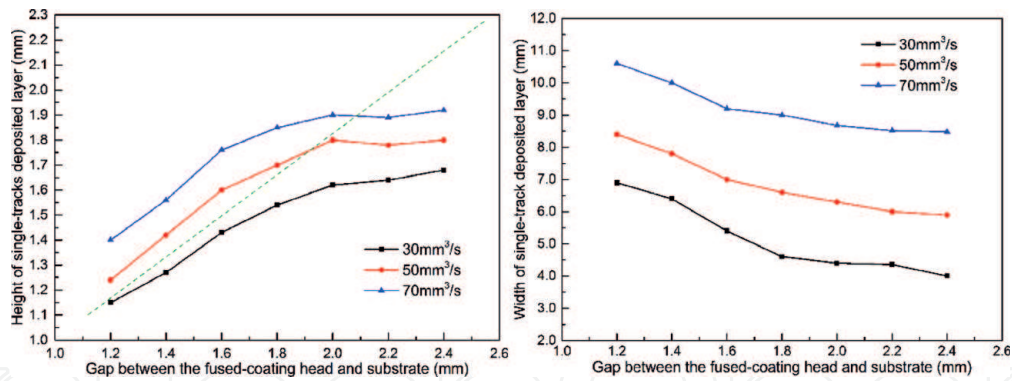*Variation of the morphology characteristics of deposited single tracks with melt flow rate.*

Figure 25.
Influence of the gap height on the morphology characteristics of single-track deposits.

MFCAM process, the area of the absorbed arc energy is heated alternatively. The residual heat in the material will be continuously accumulated from pulse to pulse. The heat accumulation, as a function of processing parameters, is proportional to the duration of arc heat input.

When the substrate moving speed and arc heat input keep invariant, the local high-temperature range and the molten pool size should remain unchanged. However, the local melting/solidification behaviors will be partially changed with the spontaneous fusion of extruded liquid metal and the melt in the molten pool. As the melt flow rate increases, heat sink effect on the penetration depth becomes more significantly since the additional heat energy from the being extruded melt is partially transferred to the molten pool, thus the additional thermal energy actually prolongs solidification time and makes the penetration depth increase.

3.3.4 Influence of the gap height

On the other hand, the influence of the gap height between substrate and fused-coating head on the morphology characteristics of single-track deposits is also discussed, as shown in **Figure 25**. The range of melt volume flow rate is 30–70 mm^3/s. The substrate moves at a constant speed of 5 mm/s.

As illustrated in **Figure 25**, it was proved that the deposition height increases with the increase in the gap height, but the reverse is true in the deposition width. The reason for this phenomenon can be explained by researching the morphology of free surface and the thermal-flow characteristics around the fused-coating head, two main causes are pointed out: (i) liquid metal state under the condition of being squeezed, (ii) the adhesion properties of the melt around the fused coating head.

Squeezed flow behaviors of the liquid metal within a narrower gap plays a dominant role in MFCAM process, the penetration may be deeper than that in a simple thermocapillary shear flow because of the presence of pressure gradients. In this situation, the flow direction of the melt transforms from the rear toward the lateral, thus the deposition widths achieve actually increase. Meantime, it is also found that a larger gap easily leads to a higher and narrower deposition layer. This is attributed to the fact that as the gap is sufficiently large, the thermocapillary force will become not evidence, while the gravity effect and the adhesion between liquid metal and fused-coating head become remarkable.

4. Conclusions

Two multi-physics numerical models were developed to investigate the three-dimensional transient dynamics of the melt in deposition processes associated with

SLM and MFCAM. The geometries of single-track depositions under both laser- and arc-heated modes were obtained by simulations and compared with experimental observations. The molten pool motion/geometry and the computed temperature distribution from simulated results are used to analyze the formation mechanisms of deposited layers. The major findings of the current work are summarized briefly summarized as follows:

1. A randomly distributed powder bed model was established to study the effect of layer thickness and hatching spacing on the thermal behavior of AlSi10Mg molten pool. The numerical calculation results were verified by experiments.

2. The pore and balling formation mechanisms during AlSi10Mg SLM were revealed by using numerical and experimental method. The cross-section of the part produced by SLM using the laser power of 180 W and scan speed of 1000 mm/s showed a fine microstructure without any apparent pores. The larger hatch spacing may result in poor inter-track bonding inducing the inter-track pores. Also, the larger powder layer thickness is one of the key factors in inducing the inter-layer pores. In order to produce a fully dense AlSi10Mg part without any apparent pore and balling defects, the laser power of 180 W, the scanning speed of 1000 mm/s, the powder layer thickness of 35 μm, and the hatch spacing of 50 μm are proposed during SLM.

3. The whole evolution processes of the deposited layer morphology in MFCAM process could be generally divided into four stages. There are local fluctuations of the profile of liquid-solid interface, which can be attributed to the spatial-temporal fluctuations of fluid momentum in pulsed current mode. The spatial variability of the liquid-solid interface results in the variability in the solidification parameters, which impact the deposited layer morphology.

4. The substrate moving speed can significantly affect the morphology of deposited layers. Width and height of deposited layers usually decrease with the increase of substrate moving speed.

Acknowledgements

Author details

Zhengying Wei* and Jun Du
The State Key Laboratory for Manufacturing Systems Engineering, Xi'an Jiaotong University, Xi'an, China

*Address all correspondence to: zywei@mail.xjtu.edu.cn

IntechOpen

References

[1] Tofail SAM, Koumoulos EP, Bandyopadhyay A, Bose S, O'Donoghue L, Charitidis C. Additive manufacturing: Scientific and technological challenges, market uptake and opportunities. Materials Today. 2018;**21**:22-37

[2] Wohlers TT, Caffrey T. Wohlers Report 2014: Additive Manufacturing and 3D Printing State of the Industry Annual Worldwide Progress Report. Fort Collins, Colorado: Wohlers Associates, Inc.; 2014

[3] King WE, Anderson AT, Ferencz RM, Hodge NE, Kamath C, Khairallah SA, et al. Laser powder bed fusion additive manufacturing of metals; physics, computational, and materials challenges. Applied Physics Reviews. 2015;**2**:041304

[4] DebRoy T, Wei HL, Zuback JS, Mukherjee T, Elmer JW, Milewski JO, et al. Additive manufacturing of metallic components—Process, structure and properties. Progress in Materials Science. 2018;**92**:112-224

[5] Babu SS. Scripta Viewpoint Set: Materials science aspects related to additive manufacturing. Scripta Materialia. 2017;**135**:97-99

[6] O'Regan P, Prickett P, Setchi R, Hankins G, Jones N. Metal based additive layer manufacturing: Variations, correlations and process control. Procedia Computer Science. 2016;**96**:216-224

[7] Herzog D, Seyda V, Wycisk E, Emmelmann C. Additive manufacturing of metals. Acta Materialia. 2016;**117**: 371-392

[8] Hebert RJ. Viewpoint: Metallurgical aspects of powder bed metal additive manufacturing. Journal of Materials Science. 2016;**51**:1165-1175

[9] Yusuf SM, Gao N. Influence of energy density on metallurgy and properties in metal additive manufacturing. Materials Science and Technology. 2017;**33**:1269-1289

[10] Francois MM, Sun A, King WE, Henson NJ, Tourret D, Bronkhorst CA, et al. Modeling of additive manufacturing processes for metals: Challenges and opportunities. Current Opinion in Solid State and Materials Science;**21**:198-206

[11] Bikas H, Stavropoulos P, Chryssolouris G. Additive manufacturing methods and modelling approaches: A critical review. The International Journal of Advanced Manufacturing Technology. 2015;**83**:1-17

[12] Mukherjee T, Manvatkar V, De A, DebRoy T. Dimensionless numbers in additive manufacturing. Journal of Applied Physics. 2017;**121**:064904

[13] Wei P, Wei Z, Chen Z. Thermal behavior in single track during selective laser melting of AlSi10Mg powder. Applied Physics A. 2017;**123**:604

[14] Wei P, Wei Z, Chen Z. Numerical simulation and parametric analysis of selective laser melting process of AlSi10Mg powder. Applied Physics A. 2017;**123**:540

[15] Roux JN. Geometric origin of mechanical properties of granular materials. Physical Review E. 2000; **61**(6):6802

[16] Rong G, Liu G, Hou D, Zhou C. Effect of particle shape on mechanical behaviors of rocks: A numerical study using clumped particle model. Scientific World Journal. 2013;**2013**: 289215-589215

[17] Hirt CW, Nichols BD. Volume of fluid (VOF) method for the dynamics of free boundaries. Journal of Computational Physics. 1981;**39**:201-225

[18] Stacy SC, Zhang X, Pantoya M, Weeks B. The effects of density on thermal conductivity and absorption coefficient for consolidated aluminum nanoparticles. International Journal of Heat and Mass Transfer. 2014;**54**: 595-599

[19] Dai K, Shaw L. Finite element analysis of the effect of volume shrinkage during laser densification. Acta Materialia. 2005;**53**:4743-4754

[20] Semak V, Matsunawa A. The role of recoil pressure in energy balance during laser materials processing. Journal of Physics D: Applied Physics. 1999;**30**: 2541

[21] Min HC, Yong CL, Farson D. Simulation of weld pool dynamics in the stationary pulsed gas metal arc welding process and final weld shape. Welding Journal. 2006;**85**:271-283

[22] Masmoudi A, Bolot R, Coddet C. Investigation of the laser–powder–atmosphere interaction zone during the selective laser melting process. Journal of Materials Processing Technology. 2015;**225**:122-132

[23] Dou L, Yuan ZF, Li JQ, Wang X. Surface tension of molten Al-Si alloy at temperatures ranging from 923 to 1123 K. Chinese Science Bulletin. 2008;**53**: 2593-2598

[24] Gu DD, Wang Z, Shen Y, Li Q, Li Y. In-situ TiC particle reinforced Ti–Al matrix composites: Powder preparation by mechanical alloying and selective laser melting behavior. Applied Surface Science. 2009;**255**:9230-9240

[25] Goldak J, Chakravarti A, Bibby M. A new finite element model for welding heat sources. Metallurgical and Materials Transactions B. 1984;**15**: 299-305

[26] Desai RS, Bag S. Influence of displacement constraints in thermomechanical analysis of laser micro-spot welding process. Journal of Manufacturing Processes. 2014;**16**: 264-275

[27] Cho DW, Lee SH, Na SJ. Characterization of welding arc and weld pool formation in vacuum gas hollow tungsten arc welding. Journal of Materials Processing Technology. 2013; **213**:143-152

[28] Sreedhar U. Static GTAW: Experimental and numerical investigations and heat flux parameter estimation [PhD thesis]. Montpellier, France: Universit'e Montpellier-II; 2014

[29] Cho DW, Na SJ, Cho MH, Lee JS. Simulations of weld pool dynamics in V-groove GTA and GMA welding. Weld World. 2013;**57**:223-233

[30] Kou S, Sun DK. Fluid flow and weld penetration in stationary arc welds. Metallurgical and Materials Transactions A: Physical Metallurgy and Materials Science. 1985;**16**:203-213